

Solid Electrolyte Interphase Formation on Anatase TiO₂ Nanoparticle-Based Electrodes for Sodium-Ion Batteries

Andreas Siebert,* Xinwei Dou, Raul Garcia-Diez, Daniel Buchholz, Roberto Félix, Evelyn Handick, Regan G. Wilks, Stefano Passerini, and Marcus Bär



Cite This: *ACS Appl. Energy Mater.* 2024, 7, 125–132



Read Online

ACCESS |



Metrics & More



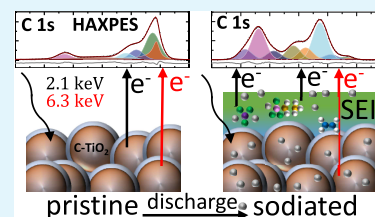
Article Recommendations



Supporting Information

ABSTRACT: Carbon-coated anatase TiO₂ nanoparticles are a promising anode material for sodium-ion batteries, theoretically providing a satisfactory capacity combined with a relatively low cost, environmental friendliness, and high-rate capability. Nondestructive, depth-resolved hard X-ray photoelectron spectroscopy (HAXPES) is exploited to reveal the composition profile of the solid electrolyte interphase (SEI) that forms during the first sodiation (discharge) cycle and that has been determined to be (on average) 6 nm thick. Sodium chloride (NaCl), sodium fluoride (NaF), sodium carbonate (Na₂CO₃), sodium alkyl carbonates (NaCO₃-R), poly(ethylene oxide) (PEO), sodium hydroxide (NaOH), sodium ions, and hydrocarbons have been identified as the major species within the SEI, with a higher hydrocarbon concentration near the SEI/electrode interface and a higher sodium-ion concentration at the SEI surface. These findings give detailed insights into the complex interplay taking place at the electrolyte/TiO₂ nanoparticle interface during the sodiation/desodiation (discharging/charging) processes, paving the way for a deliberate optimization.

KEYWORDS: titanium dioxide, sodium-ion battery, hard X-ray electron spectroscopy, anode, SIB



1. INTRODUCTION

Driven by the worldwide increasing demand for energy storage systems for electric vehicles, portable devices, and storage systems for the fluctuating output of some sustainable energy sources, sodium-ion batteries (SIBs) represent a promising electrochemical energy storage technology independent from limited lithium resources and thus represent an alternative to the current state-of-the-art lithium-ion battery (LIB) technology. SIB raw materials are more abundant, geographically more homogeneously distributed, and of lower cost than LIB materials, mitigating economical and geopolitical risks.^{1,2}

Among several promising anode materials for application in SIBs, titanium oxides, particularly anatase TiO₂, so far show the best results in terms of specific capacity and cycle life compared to its allotropes rutile, brookite, or amorphous TiO₂.^{3–15} Furthermore, extensive effort has been invested into tailoring the anode materials' morphologies into nanostructures like nanorods, nanowires, nanotubes, nanoparticles, or microspheres.^{6,8,16–19} It was shown that reducing the nanoparticle size can increase the specific capacity and that a carbon coating can enable a higher rate capability. In this regard, an anode containing carbon-coated anatase nanoparticles (11 nm average diameter), delivered a specific capacity of 227 mAh g⁻¹ at 0.1 C.⁶

Due to the large surface-to-volume ratio of nanostructured electrodes, important parameters defining their performance are the electrolyte compatibility and those controlling the formation of a stable solid electrolyte interphase (SEI) layer.²⁰ The SEI is a thin layer that forms at the electrode surface

mainly due to the degradation of the used electrolyte solvents and anion salts, which are unstable at typical working potentials. The layer separates the electrode from the liquid electrolyte, passivating the electrode ideally enabling a stable battery performance in an increased voltage window, thus governing important parameters like the battery lifetime, rate capability, and practical accessible capacity.²¹

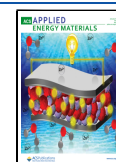
The properties of the SEI depend largely on the type of electrolyte. Anatase TiO₂ nanoparticle-based electrodes have been tested with various electrolytes composed of salts like sodium bis(trifluoromethanesulfonyl)imide (NaTFSI), sodium perchlorate (NaClO₄), or sodium hexafluorophosphate (NaPF₆) dissolved in mixtures of bis(2-methoxyethyl) ether (DEGDME), propylene carbonate (PC), dimethyl carbonate (DMC), fluoroethylene carbonate (FEC), ethylene carbonate (EC), and even ionic-liquid based electrolytes,^{6,8,9,18,21–23} though NaClO₄ dissolved in a 1:1 volume mixture of EC/PC has so far demonstrated the best electrochemical performance in SIBs.⁸ The formed SEI stops further degradation of the electrolyte at the electrode surface, preventing an additional loss of charge, resulting in a low Coulombic efficiency.

Received: September 14, 2023

Revised: December 4, 2023

Accepted: December 6, 2023

Published: December 27, 2023



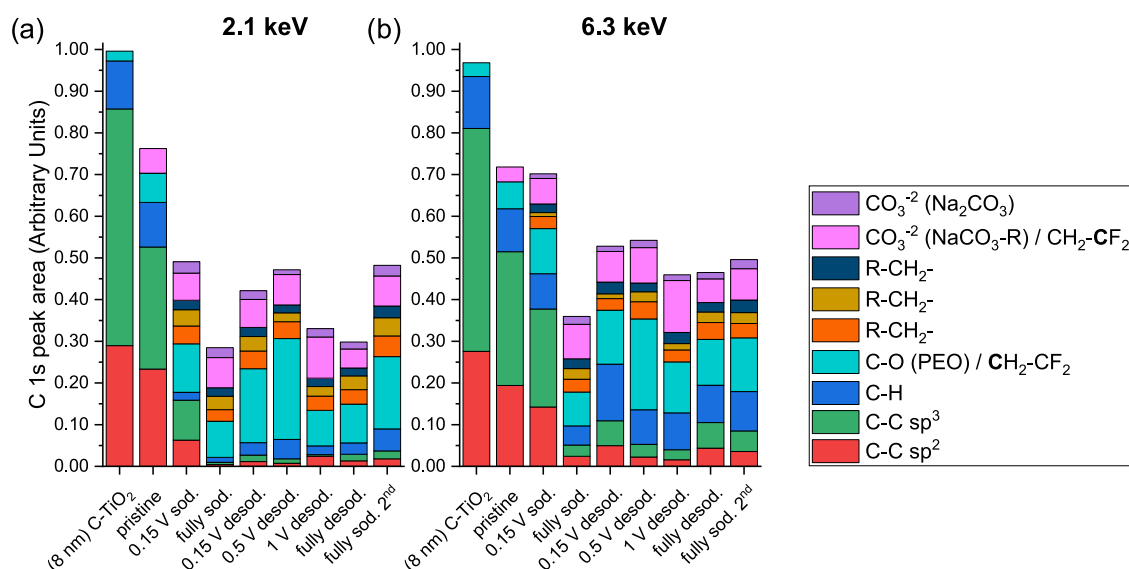


Figure 1. Area of the C 1s core level and its relative spectral contributions assigned to different chemical carbon environments based on the HAXPES data measured with photon energies of (a) 2.1 keV and (b) 6.3 keV (see Figure S3). For the studied carbon-coated TiO₂ nanoparticle reference sample (“(8 nm) C-TiO₂”), the pristine, and the differently discharged (sodiated) samples, we find indications for the presence of C–C sp² and sp³ species (presumably from the carbon coating and the employed C65 conductive agent), C–H bonds, CH₂–CF₂ (from the PVDF binder) overlapping with the C–O bond (from PEO and/or surface contamination) spectral contributions, different R–CH₂–type species (alkyl chains bond to different functional groups), overlapping spectral contributions attributed to NaCO₃–R (sodium alkyl carbonate or bicarbonate like species) and/or CH₂–CF₂ bonds, and sodium carbonate (Na₂CO₃). R relates to H or alkyl groups with different chain lengths.

However, relatively low Coulombic efficiencies of around 40% have been reported for SIBs based on TiO₂ anodes. The reason for this behavior and the insertion mechanism of sodium ions was recently elucidated, showing that the majority of sodium ions are trapped irreversibly in a new amorphous anode structure that the initial anatase TiO₂ structure is converted into during the first sodiation cycle, while in comparison only small amounts of sodium are lost in side reactions like the SEI layer formation.²⁴ The underlying reason for this observation is suggested to be studied by hard X-ray photoelectron spectroscopy (HAXPES) measurements, which can probe the electrode material buried below the formed SEI layer. Using different (high) excitation energies, nondestructive depth-resolved chemical structure information can be gained while exploiting and varying the larger probing depths related to the larger electron inelastic mean free path (IMFP) for high kinetic energy photoelectrons compared to regular (soft) X-ray photoelectron spectroscopy (XPS). The large amount of XPS studies about the SEI formation in LIBs^{25–31} combined with the (in that sense) small translational gap between LIB and SIB technologies due to comparable chemical reactions and data evaluation analogies^{2,32} promises rapid knowledge gain.

In this work, we report on a comprehensive, nondestructive, depth-resolved HAXPES study focusing on the formation, composition, and evolution of the SEI layer on carbon-coated anatase TiO₂ nanoparticle-based anodes for SIBs, giving insights into the chemical properties of this interface and the sodiation/desodiation (discharging/charging) effects on the buried TiO₂-based anode.

2. RESULTS AND DISCUSSION

The effects of sodiation and desodiation of carbon-coated anatase TiO₂ nanoparticle-based anodes have been studied with HAXPES measurements for eight different electrode samples each at a different discharge or charge state, and for

two anatase TiO₂ reference samples: carbon-coated TiO₂ nanoparticles with an average particle diameter of (8 ± 3) nm and uncoated TiO₂ nanoparticles with an average particle size of (15 ± 2) nm, as derived by X-ray diffraction (XRD) and small-angle X-ray scattering measurements.^{6,33} A schematic overview of the (dis)charge states of the measured samples is provided in Figure S1 (see Section 1 of the Supporting Information), while Figure S2 depicts the respective measured HAXPES survey spectra. The focus of the investigation was put on the determination of the composition profile and the monitoring of the formation of the SEI layer on top of the anode samples while gaining complementary insights of the sodium insertion mechanism into the electrode. Therefore, the C 1s, O 1s, F 1s, Na 1s, Cl 2s, Cl 2p, and Ti 2p core levels were measured with two different excitation energies to allow for the acquisition of depth-dependent information about the SEI layer (composition and formation) and the underlying TiO₂-based electrode. Additionally, the Na KLL Auger spectra has been measured with an excitation energy of 2.1 keV.

A detailed evaluation of the core levels and Na KLL spectra can be found in Section 2 of the Supporting Information. The attribution of specific spectral contributions to the core levels derived from the thorough peak fit analysis to different chemical species is based on reported reference peak positions presented in Tables S1 and S5 and on a comparison of the expected relative peak areas (RPAs) for selected species and their spectral contributions to the studied core levels. To do so, the fitted peak areas have been corrected for the transmission function of the electron analyzer, the photoionization cross-section, and the photoelectrons’ inelastic mean free path (IMFP). To allow for easy comparison, the (nominal) stoichiometry of the assigned species has also been considered (see Section 3 of the Supporting Information for more details).

Figure 1 shows the relative quantity of C-containing species as derived from the analysis of the C 1s HAXPES core level measured with 2.1 and 6.3 keV excitation energies depicted in

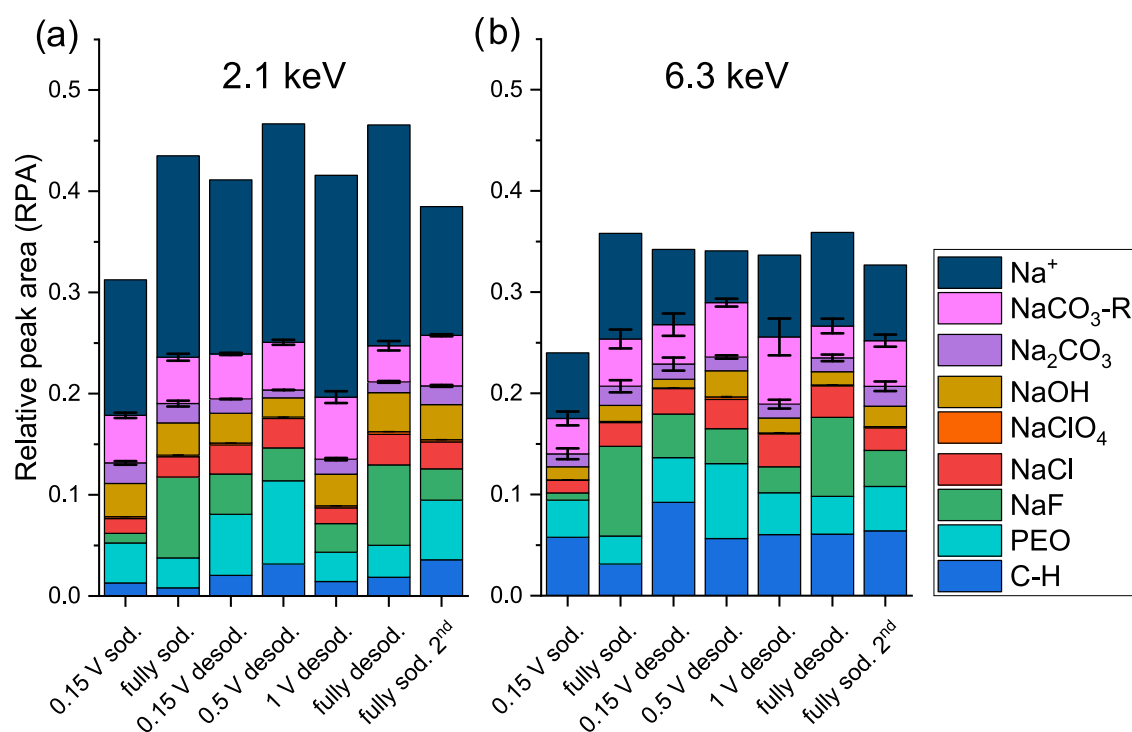


Figure 2. Comparison of the relative amount of the identified chemical species contributing to the SEI for all discharged (sodiated)/charged (desodiated) TiO_2 nanoparticle anode samples as derived from the C 1s, O 1s, F 1s, Cl 2s and 2p, and Na 1s HAXPES spectra recorded with photon energies of (a) 2.1 keV and (b) 6.3 keV. For the $\text{NaCO}_3\text{-R}$, Na_2CO_3 , and NaClO_4 contributions, the average between the relative peak areas of the species in the O 1s and the C 1s (respectively Cl 2s) core levels has been taken, and the depicted error bar represents the respective difference.

Figure S3. The carbon-coated reference sample (“(8 nm) C- TiO_2 ”) is composed of major contributions from C–C sp^2 and sp^3 bonds related to the carbon coating and only minor contributions preliminarily attributed to surface contamination related to adsorbed C–H and C–O. The pristine electrode C 1s spectrum is very similar to that of the reference sample, with additional contributions related to $\text{CH}_2\text{-CF}_2$ bonds of the poly(vinylidene fluoride) (PVDF) binder, giving rise to two additional spectral C 1s components (see **Figure S3**). The ratio of sp^2 and sp^3 bonds is slightly changed due to the conductive carbon added to the pristine electrode sample.

The following samples were in contact with the electrolyte and were discharged/charged (i.e., sodiated/desodiated) to certain potentials (see **Figure S1**). Starting with the 0.15 V sodiated (discharged) sample, small contributions related to the formed SEI are present. There are contributions from C–H bonds, related to hydrocarbons, C–O bonds, attributed to $\text{H-(O-CH}_2\text{-CH}_2)_n\text{-OH}$ poly(ethylene oxide) (PEO), R– $\text{CH}_2\text{-}$ bonds corresponding to the last carbon atom of alkyl chains bound to different functional groups, like NaCO_3 , NaOH, or Na^+ . Furthermore, spectral $\text{NaCO}_3\text{-R}$ - and Na_2CO_3 -related bond contributions are present, corresponding to sodium alkyl carbonates or bicarbonate and to sodium carbonate (R relates to H or alkyl groups with various chain lengths, which can result in different amounts of additional hydrocarbon C–H bond-related spectral intensity). While the spectral C 1s contribution of these SEI species is relatively small compared to the carbon coating-related C–C sp^2 and sp^3 spectral features for the 0.15 V sodiated sample, it greatly increases for the other discharged/charged samples. The growth of the SEI on top of the electrode attenuates the signal contribution from the species related to the underlying electrode, causing a

pronounced decrease in the C–C sp^2 - and sp^3 -related spectral C 1s contributions. The C–H-related spectral contribution to the more bulk sensitive 6.3 keV excited C 1s data is larger than the more surface sensitive 2.1 keV spectra for all discharged/charged samples, indicating that this signal is not primarily related to adventitious hydrocarbon surface contaminants.³⁴ Polyolefins $(\text{CH}_2)_n$, which may form due to polymerization of unsaturated hydrocarbons that are a degradation product of EC and PC,^{28,35} have been reported to form at the outermost side of the SEI close to the electrolyte in case of carbon and lithium electrodes for LIBs^{26,36,37} because of their (partial) solubility in the electrolyte. They are not ionically conductive and therefore can restrict/limit charge carrier transport leading to an inferior cell performance.³⁵ However, they are soft and can fill cavities and add flexibility to the SEI,^{35,38} which may be considered to be beneficial. Our depth-dependent HAXPES results, however, indicate a different scenario for carbon-coated TiO_2 nanoparticle anodes, suggesting the formation and accumulation of hydrocarbons at the SEI/electrode interface (instead of the electrolyte/SEI interface), likely related to the adsorption of unsaturated hydrocarbons at the anode surface during the first stages of SEI formation.

The observation of PEO is attributed to the ring opening of EC during the first sodiation of TiO_2 with subsequent polymerization, where CO_2 is formed as a side product as previously corroborated by gas chromatography measurements of nanoparticle-based SIB anodes.⁷ The presence of PEO can also lead to the subsequent formation of oxalate type species.^{2,39,40}

As the presence of alkoxides has been reported for a system containing an EC:PC electrolyte,³² the formation of small amounts of alkoxides cannot be excluded in this study and

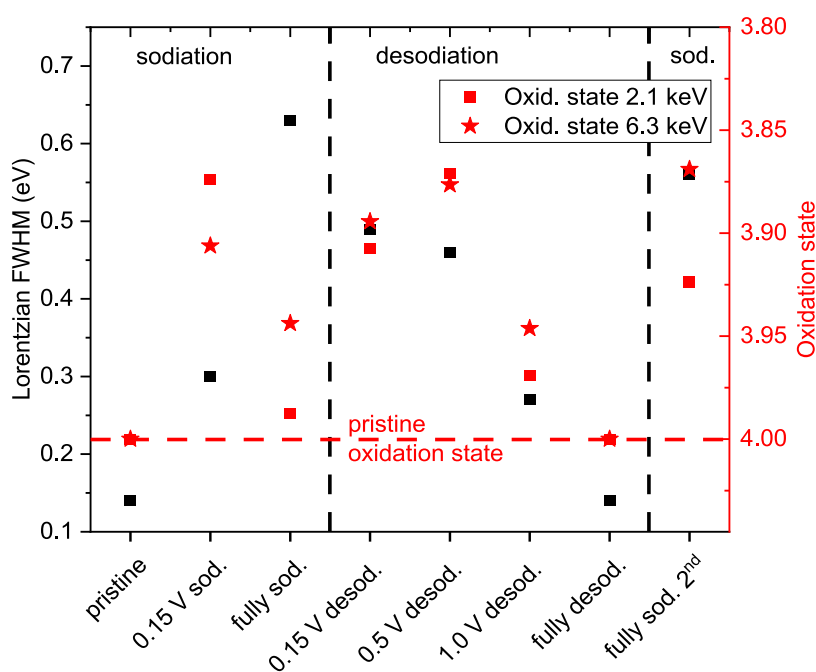


Figure 3. Lorentzian FWHM of the Ti 2p_{3/2} peaks and the derived average Ti oxidation state for both excitation energies of anatase TiO₂ nanoparticle-based anode samples at different stages during discharge (sodiation)/charge (desodiation). The Lorentzian FWHM is increasing, and the Ti oxidation state is mainly decreasing during sodiation and vice versa during desodiation. A red dotted line indicates the pristine oxidation state as well as the calculated Lorentzian FWHM for the Ti 2p_{3/2} core level peaks based on the core-hole lifetime (0.22 ± 0.06 eV).⁴⁷

might be related to the hydrolysis of EC, because of traces of water present in the electrolyte or related to the presence of small amounts of moisture during sample handling.

In addition to the carbon-containing species in the SEI, there are additional species contributing to the SEI, which can be revealed evaluating the other measured core levels, O 1s, F 1s, Cl 2s and 2p, and Na 1s (see Figures S4–S8).

In Figure 2, the relative amount of the identified chemical species contributing to the SEI is presented for both excitation energies, based on the peak assignment in the C 1s, O 1s, F 1s, Cl 2s and 2p, and Na 1s spectra depicted in Figures S3–S8. The SEI layer is mainly composed of NaF, NaCl, NaClO₄, NaOH, and Na⁺ ions, in addition to the already identified hydrocarbon, PEO, Na₂CO₃, and NaCO₃-R SEI contributions. The assignment of the spectral contributions to the C 1s, O 1s, F 1s, Cl 2s and 2p, and Na 1s core levels to the various chemical species has been done by comparing to reference binding energies from the literature (Tables S1–S5), cross checked by comparing the RPAs for each species in the respective core levels as shown in Figures S10 and S15, for TiO₂, NaClO₄, NaCl, NaF, Na₂CO₃, and NaCO₃-R (see Section 3 of the Supporting Information for more details).

In the Na 1s core level spectra, the energy differences between different species are relatively small; hence, the Na 1s spectra have been evaluated together with the Na KLL Auger spectra to be able to consult the calculated modified Auger parameter (presented in the Wagner plot in Figure S9), which gives more dependable information about the present Na species. Critically, the modified Auger parameter is unaffected by shifts due to doping, charging, etc., and a particular chemical species will fall on the same diagonal in the Wagner plot. The plot suggests that the already identified Na₂CO₃ and NaCO₃-R together with NaCl, NaF, NaOH, and Na⁺ ions are the dominant sodium species in the SEI. The presence of

significant amounts of metallic sodium and sodium oxide in the SEI can be excluded based on this evaluation.

The presence of NaF can be related to the (partial) degradation of the PVDF binder. Sodium or lithium fluoride formation is observed in nearly every fluorine-containing battery^{27,30,36,41,42} and additionally a (partial) degradation (dehydrofluorination) of PVDF has already been reported for other systems.^{32,43,44} The degradation of the binder is critical in terms of battery operation since the loss of its cohesive properties might result in the dissolution of active electrode material and a loss of specific capacity.

Along with the degradation of the binder, a degradation of the electrolyte salt NaClO₄ to NaCl additionally leads to an oxygen gas release, which has been previously detected by gas chromatography measurements.⁷ Spectral proof of the presence of chemically adsorbed O₂ in the spectra of the O 1s might be overshadowed by the overlapping sodium hydroxide peak. The release of O₂ could also correspond to oxygen losses occurring due to the structural rearrangement of the anatase TiO₂ anode material, reported to be in a range between 5 and 7%.²⁴ An additional (partially extrinsic) reason for the degradation of NaClO₄ could be the exposure to highly intense X-rays during the HAXPES measurements, similarly reported in the literature^{32,45} and as can be seen in Figure S7b, by the increasing intensity of the NaCl peak with measurement time, i.e., increasing radiation dose. Exposure of sodium oxalate (formed out of sodium ions and CO₂ released during EC ring opening) to traces of water might have led to the formation of sodium hydroxide and bicarbonate. The sodium hydroxide may have additionally favored the above-discussed (partial) degradation of the PVDF binder.⁴⁶

The aforementioned higher amount of hydrocarbons in the more bulk sensitive HAXPES measurements (performed by using a higher excitation energy) is also visible in Figure 2. While most of the other species seem not to show a

pronounced depth-dependent distribution profile in the SEI, we find a significantly increased amount of Na⁺ ions in the surface compared with the bulk sensitive measurements. This is in contrast to the expected high Na⁺ ion concentration inserted into the electrode during discharge. However, looking at the small changes of the average Ti oxidation state for the discharged/charged samples (see Figure 3) from its original +4 pristine state obtained from the Ti 2p spectra (see Figure S16), which is in contrast to previous operando measurements,²⁴ one can conclude that a large amount of Na⁺ ions have superficially left the electrode after battery disassembly. Ions subsequently migrated through the SEI layer toward the sample surface could explain the high sodium-ion concentration observed in the SEI surface. Additional Na⁺ ions originating from electrolyte residual might be present at the SEI surface as well, offering another explanation for the observation of a high surface content of Na⁺ ions.

The concentrations of PEO, NaF, NaCl, NaClO₄, NaOH, Na₂CO₃, and Na₂CO₃-R for the 2.1 keV measurements are for some samples lower and for some samples higher compared to the 6.3 keV measurements, i.e., their concentration depth profile is ambiguous. Despite some significant changes in the individual SEI species concentrations between the investigated samples, we do not see a clear trend of a species concentration profile following the state of charge or discharge of the anode.

In Figure 3, the oxidation state of Ti in the electrode samples for the two excitation energies is presented together with the Lorentzian width (kept the same for both excitation energies). The Lorentzian width displays a clear correlation with the electrode state of discharge (sodiation)/charge (desodiation) of the samples. During sodiation, an increase of the Lorentzian width can be observed, which is nearly completely reversed during desodiation, analogously to Ti 2p_{3/2} peak broadening reported for Li inserted into TiO₂ and Na into TiS₂.^{48,49} For the Li insertion, the change in the natural width of the TiO₂ component was related to a subsequent distortion of the lattice, creating several slightly shifted Ti 2p_{3/2} components or due to an inhomogeneous Li insertion resulting in undefined stoichiometric lithium-inserted TiO₂ nanocrystals.⁴⁸ In contrast, the Ti 2p_{3/2} peak broadening of TiS₂ was explained by a final state effect, caused by an additional shielding from the itinerant electrons injected in the valence band.⁴⁹ This explanation seems more plausible in our case since structural changes are not likely (completely) reversible and hence lack to explain the FWHM decrease during desodiation to its original value. For the same reason, a peak broadening due to the irreversible structural changes in the anatase TiO₂ electrode observed during the first sodiation cycle reported previously can be excluded.^{5,7,19,22,24,33,50}

Due to the Na insertion in the electrode (i.e., sodiation) upon discharging and the desodiation of the electrode during charging, the (average) oxidation state of the titanium in the TiO₂ nanoparticle anode is expected to change in a discharge (sodiation)/charge (desodiation) cycle. Indeed, we observe the (average) titanium oxidation state mainly decreases during sodiation and increases again during desodiation (with the first fully sodiated sample being an apparent outlier not following this trend, see Figure 3). In the corresponding Ti 2p detail spectra depicted in Figure S16, the appearance of a Ti³⁺ species can be observed during sodiation with no indication for the formation of Ti metal or TiO. However, the changes of the (average) oxidation state are relatively small, with a minimum value of Ti^{+3.87} observed for the sample that had been fully

sodiated for the second time. This would correspond to a maximum of 0.13 inserted Na⁺ per formula unit TiO₂. This is much smaller than the values derived from electrochemical measurements, reporting values of up to 0.69 Na⁺ per formula unit TiO₂⁷ and the more pronounced oxidation state changes observed in a previous study based on operando XANES measurements.²⁴ The discrepancy might be explainable with the lower information depth of the HAXPES compared to the XANES measurements and by the ex situ conditions of our experiment. In fact, a newly formed amorphous TiO₂ structure containing 0.18 irreversible trapped Na⁺ ions per formula unit TiO₂ reported in the literature might only form in the bulk of the anode, since the pressure and volume increase due to Na⁺ ion insertion is probably mitigated at the surface.²⁴

Interestingly, the Lorentzian FWHM broadening of the Ti 2p_{3/2} core level peaks presented in Figure 3 is more consistently related to the state of discharge (sodiation)/charge (desodiation) compared to the calculated oxidation state, i.e., although (our seeming outlier) the first fully sodiated sample shows a very low deviation from the pristine titanium oxidation state, the Lorentzian FWHM is significantly increased compared to that of the pristine sample and is similar to the value for the sample that had been fully sodiated for a second time (and does show the largest deviation from the pristine titanium oxidation state). Hence, it might be beneficial for future studies to carefully monitor the Ti 2p_{3/2} Lorentzian FWHM which seems to be more sensitive to changes in the titanium oxidation state (via changes in the shielding of the core hole created by the photoemission process) than conventional spectral fit analysis.

Based on the peak area of the TiO₂ species-related spectral contribution to the Ti 2p_{3/2} and O 1s spectra recorded with photon energies of 2.1 and 6.3 keV (depicted in Figure S17) and assuming that the SEI is represented by a compact layer of Na₂CO₃, the thickness of the SEI for the studied electrodes at different charging states can be estimated and is shown in Figure S18 (see Section 4 of the Supporting Information for more details). The SEI is in average (6 ± 1) nm thick comparable with previous SEI thickness estimations for carbonate based electrolytes in SIBs of 5–10 nm,^{39,51} without any pronounced variations except for the 1 V desodiated and second fully sodiated samples, for which we find the maximum (9 nm) and minimum (<4 nm) SEI thickness values, respectively. In contrast to reports of an SEI layer formed on Na₂Ti₃O₇ electrodes using the same electrolyte as used in this study, becoming unstable upon charging,³² our results suggest a relatively stable SEI without any systematic charge state dependent changes in thickness. Furthermore, the mainly unchanged chemical composition after the first cycle, prominently indicated by the mostly unchanged C 1s and O 1s spectra of the fully desodiated and the subsequently second fully sodiated samples (see Figures S3 and S4), shows the formation of a stable SEI during the first cycle, which is mainly unaltered afterward.

3. CONCLUSIONS

In this paper, we use nondestructive depth-resolved HAXPES measurements to study the interface between carbon-coated anatase TiO₂ nanoparticle-based anodes and the formed SEI layer. We find that the SEI forms during the first discharge (sodiation)/charge (desodiation) cycle and mainly consists of hydrocarbons, PEO, sodium alkyl carbonates, sodium carbonate, and sodium hydroxide presumably due to the

Table 1. Voigt, Lorentzian, and Gaussian FWHM Used for the Fits of the Core Level Spectra of the TiO₂-Based Electrode Samples^a

core level	Voigt FWHM [eV]	Gaussian FWHM [eV]	Lorentzian FWHM [eV]	cal. Lorentzian FWHM [eV]	difference Lorentzian [eV]
C 1s	1.14	1.14	5×10^{-10}	0.06 ⁵⁶	-0.06
O 1s	1.11	1.08	0.06	0.15 ⁵⁶	-0.09
F 1s	1.38	1.20	0.31	0.2 ⁵⁶	0.11
Cl 2s	2.33	1.30	1.55	1.58 ± 0.47 ⁴⁷	-0.12
Na 1s	1.30	1.17	0.26	0.30 ± 0.03 ⁴⁷	-0.04
Ti 2p _{3/2}	1.16–1.46	1.08	0.14–0.63	0.22 ± 0.06 ⁴⁷	

^aFor comparison, values of the calculated Lorentzian FWHM using the core-hole lifetime from the literature are given, and the difference to the fitting values are calculated.

decomposition of EC and PC. Furthermore, NaCl and NaF are present in the SEI due to the (partial) reduction of the electrolyte salt and PVDF binder. This results in the formation of a stable SEI layer of around a 6 nm thickness. The deeply buried interface region of the SEI and the electrode contains a higher hydrocarbon concentration compared to that of the rest of the SEI, which is attributed to the adsorption of unsaturated hydrocarbons (originating from the degradation of the electrolyte) at the electrode surface during the initial stage of SEI formation. The insertion of sodium into anatase TiO₂ is responsible for the formation of Ti³⁺ derived states, while no TiO or Ti metal can be detected in agreement with previous works.

The amount of sodium corresponding to the reduced (average) titanium oxidation state from operando results significantly differs from that obtained from electrochemical results, likely due to (superficial) sodium losses occurring upon handling of the specimen (i.e., after electrochemical cell disassembly), explaining a high amount of sodium ions at the SEI surface possibly originally present in the electrode bulk.

In summary, this work reveals the chemical structure profile of the SEI layer and its formed interface with the carbon-coated TiO₂ nanoparticle-based anode, contributing to a better understanding of the complex processes occurring at this important interface, governing critical performance parameters of the electrochemical cell.

4. EXPERIMENTAL SECTION

4.1. Electrode Preparation, Cell Assembling, and Electrochemical Characterization. Electrodes were prepared by doctor blade casting a slurry prepared by dispersing 65 wt % active material, i.e., anatase TiO₂ nanoparticles (synthesized as described elsewhere⁶ with an 8 nm average diameter), 10 wt % PVDF binder (Solef 5130) dissolved in *N*-methyl-2-pyrrolidone (NMP) and 25 wt % carbon accounting for the carbon coating, and the conductive agent (SuperC65, IMERYS, Switzerland) on dendritic copper foil (Schlenk) as a current collector. After drying at 60 °C overnight in an oven (Binder), 12 mm diameter electrodes were punched and dried again for 24 h at 120 °C under vacuum.

Swagelok cells containing the prepared electrodes have been assembled with a sheet of Whatman glass fiber as a separator drenched in the electrolyte, a 1 M solution of NaClO₄ (98%, Sigma-Aldrich) solved in a 1:1 mixture by volume of ethylene carbonate (UBE) and propylene carbonate (Sigma-Aldrich) and sodium metal used as the counter and reference electrode. The final prepared cells were cycled with a VMP3 Potentiostat in a voltage range between 0.05 and 2.0 V with a constant current until the selected potential before disassembling. The cell assembling and disassembling have been performed in a glovebox with a water and oxygen content of less than 0.1 ppm. The disassembled TiO₂-based electrodes have been carefully rinsed in dimethyl carbonate (DMC, 99.9%, Sigma-Aldrich) and transferred in airtight containers. DMC was chosen for the rinsing

due to its rather low dielectric constant, which minimizes the dissolution of inorganic compounds in the SEI, while it still removes the salt residue on the electrode surface. The final sample preparation at the beamline was performed in an Ar₂-filled glovebox with a water and oxygen level below 1 ppm, and the sample transfer into the vacuum system was realized using an Ar₂-filled glove bag.

4.2. HAXPES Measurements. The HAXPES measurements have been performed at the HiKE endstation⁵² located at the BESSY II KMC-1 beamline⁵³ (beam focus size 0.1 × 0.1 mm²)⁵⁴ at HZB having a base pressure <1 × 10⁻⁸ mbar. Multiple diffraction orders (i.e., 2100 eV in the first order and 6300 eV in the third order) of the Si (111) crystal pair of the double crystal monochromator have been used to select excitation energies.⁵³ All spectra have been fitted with Voigt functions accounting for the convolution of Gaussian-shaped experimental resolution and Lorentzian-shaped core-hole lifetime broadening contributions, except for the C–C sp² contribution to the C 1s spectra, which was fitted with a Doniach–Sunjic profile to account for its semi-metallic nature. The same Lorentzian and Gaussian FWHM values were used for all Voigt functions of one spectrum, see Table 1, except for the Ti 2p_{3/2} spectra, where the Lorentzian width could be different, see Table S6. The Gaussian FWHM was fixed to be the same for both excitation energies, since no big difference in the experimental resolution was observed.⁵⁵

The reasonable agreement of the calculated Lorentzian FWHM compared to the fitting value and the (except for the Cl 2s) relative constant value of the Gaussian FWHM (in average 1.16 eV) attributed to the experimental resolution somewhat validates the used fitting models.

A sample independent energy calibration was achieved by measuring a clean gold foil sample and adjusting the binding energy of the Au 4f_{7/2} peak to 84.00 eV.

The positions of the Voigt functions describing different spectral contributions of one core level have been usually fixed relative to each other, i.e., the distance between the Voigt functions attributed to sodium carbonate and PEO is the same in all the fitted C 1s spectra. A difference was only allowed if one species was attributed to the electrode and the other to the SEI to allow for a shift related to a potential gradient.

The relative amount of a present species, i.e., the relative peak area (RPA) was calculated using the area of the species divided by the photoionization cross-section of the respective element, the inelastic mean free path (IMFP), and the transmission function of the electron analyzer.^{34,57–61} Values for the IMFP have been calculated with the QUASES-IMFP-TPP2M Ver. 3.0 program assuming a homogeneous Na₂CO₃ layer as an approximation for the SEI.^{57,58} Furthermore, the stoichiometry was taken into account for comparison, i.e., for example, in Figure S13, comparing the TiO₂ species in the Ti 2p_{3/2} and the O 1s spectra, the amount in the O 1s spectra is divided by a factor of 2 to allow for easier comparison. For more details on data evaluation/treatment/quantification, see the Supporting Information.

4.3. Estimation of the SEI Thickness. The thickness of the SEI layer (*x*) can be estimated using the TiO₂ signal, i.e., the RPA of the TiO₂ contribution to the O 1s and Ti 2p_{3/2} spectra for both excitation energies (*E_i*, *i* = 1,2) depicted in Figure S17 and in detail as described in the literature.⁶² These RPAs *A'_s(E₁)* and *A'_s(E₂)* have been corrected with the photoionization cross section, transmission

function of the electron analyzer, and the IMFP of the substrate, i.e., TiO₂. Furthermore, the IMFP of the top layer, i.e., the SEI is needed for both excitation energies (IMFP(E_i)) and the exit angle β under which the photons leave the sample.

$$x = \cos(\beta) \frac{\text{IMFP}_1(E_1) \cdot \text{IMFP}_2(E_2)}{\text{IMFP}_1(E_1) - \text{IMFP}_2(E_2)} \cdot \ln \left(\frac{A'_s(E_1)}{A'_s(E_2)} \right) \quad (1)$$

Using eq 1 and assuming that the IMFP of the SEI is represented by the IMFP in Na₂CO₃, the thickness of the SEI has been calculated for each sample for the TiO₂ feature of the O 1s and Ti 2p_{3/2} spectra (see Figure S18). The IMFP of Na₂CO₃ was chosen, since IMFP data are commonly available, and using the IMFP of other inorganic materials present in the samples, like NaF and NaOH, lead to very similar thicknesses (deviation of less than 5%).⁵⁷ Assuming that the SEI would be made out of pure NaCl, the thickness would increase by 25%. The IMFPs of the determined organic materials were not considered since data are less available and less reliable, but using the IMFP of polyethylene, the thickness of the SEI would increase by 35%.⁶³ Hence, the presented values may be considered as the lower bound of the SEI thickness. Any inhomogeneity of the SEI layer has not been included in the thickness estimation, which may influence the result.

■ ASSOCIATED CONTENT

SI Supporting Information

The Supporting Information is available free of charge at <https://pubs.acs.org/doi/10.1021/acsaem.3c02304>.

XPS spectra and fits; RPA comparison; effects of sodium insertion; and estimation of the SEI thickness (PDF)

■ AUTHOR INFORMATION

Corresponding Author

Andreas Siebert – Interface Design, Helmholtz-Zentrum Berlin für Materialien und Energie GmbH (HZB), 12489 Berlin, Germany; Present Address: Advanced Light Source, Lawrence Berkeley National Laboratory, 1 Cyclotron Road, Berkeley, California 94720, United States; orcid.org/0000-0003-2144-253X; Email: asiebert@lbl.gov

Authors

Xinwei Dou – Helmholtz Institute Ulm (HIU), D-89081 Ulm, Germany; Karlsruhe Institute of Technology (KIT), D-76021 Karlsruhe, Germany

Raul Garcia-Diez – Interface Design, Helmholtz-Zentrum Berlin für Materialien und Energie GmbH (HZB), 12489 Berlin, Germany; orcid.org/0009-0000-9374-1083

Daniel Buchholz – Helmholtz Institute Ulm (HIU), D-89081 Ulm, Germany; Karlsruhe Institute of Technology (KIT), D-76021 Karlsruhe, Germany

Roberto Félix – Interface Design, Helmholtz-Zentrum Berlin für Materialien und Energie GmbH (HZB), 12489 Berlin, Germany; orcid.org/0000-0002-3620-9899

Evelyn Handick – Interface Design, Helmholtz-Zentrum Berlin für Materialien und Energie GmbH (HZB), 12489 Berlin, Germany; orcid.org/0000-0002-9773-9981

Regan G. Wilks – Interface Design, Helmholtz-Zentrum Berlin für Materialien und Energie GmbH (HZB), 12489 Berlin, Germany; Energy Materials In-Situ Laboratory Berlin (EMIL), Helmholtz-Zentrum Berlin für Materialien und Energie GmbH (HZB), 12489 Berlin, Germany; orcid.org/0000-0001-5822-8399

Stefano Passerini – Helmholtz Institute Ulm (HIU), D-89081 Ulm, Germany; Karlsruhe Institute of Technology

(KIT), D-76021 Karlsruhe, Germany; orcid.org/0000-0002-6606-5304

Marcus Bär – Interface Design, Helmholtz-Zentrum Berlin für Materialien und Energie GmbH (HZB), 12489 Berlin, Germany; Energy Materials In-Situ Laboratory Berlin (EMIL), Helmholtz-Zentrum Berlin für Materialien und Energie GmbH (HZB), 12489 Berlin, Germany; Helmholtz-Institute Erlangen-Nürnberg for Renewable Energy (HI ERN), 12489 Berlin, Germany; Department of Chemistry and Pharmacy, Friedrich-Alexander-Universität Erlangen-Nürnberg, 91058 Erlangen, Germany; orcid.org/0000-0001-8581-0691

Complete contact information is available at: <https://pubs.acs.org/doi/10.1021/acsaem.3c02304>

Author Contributions

The manuscript was written through contributions of all authors. All authors have given approval to the final version of the manuscript.

Notes

The authors declare no competing financial interest.

■ ACKNOWLEDGMENTS

We acknowledge HZB for the allocation of synchrotron radiation beam time. Furthermore, the authors acknowledge the financial support of the Helmholtz Association.

■ REFERENCES

- Wadia, C.; Albertus, P.; Srinivasan, V. *J. Power Sources* **2011**, *196*, 1593.
- Ponrouch, A.; Monti, D.; Boschin, A.; Steen, B.; Johansson, P.; Palacín, M. R. *J. Mater. Chem. A* **2015**, *3*, 22.
- Su, D.; Dou, S.; Wang, G. *Chem. Mater.* **2015**, *27*, 6022.
- Hwang, J.-Y.; Myung, S.-T.; Sun, Y.-K. *Chem. Soc. Rev.* **2017**, *46*, 3529.
- Louvain, N.; Henry, A.; Daenens, L.; Boury, B.; Stievano, L.; Monconduit, L. *CrystEngComm* **2016**, *18*, 4431.
- Tahir, M. N.; Oschmann, B.; Buchholz, D.; Dou, X.; Lieberwirth, I.; Panthöfer, M.; Tremel, W.; Zentel, R.; Passerini, S. *Adv. Energy Mater.* **2016**, *6*, No. 1501489, DOI: [10.1002/aenm.201501489](https://doi.org/10.1002/aenm.201501489).
- Wu, L.; Bresser, D.; Buchholz, D.; Giffin, G. A.; Castro, C. R.; Ochel, A.; Passerini, S. *Adv. Energy Mater.* **2015**, *5*, No. 1401142, DOI: [10.1002/aenm.201401142](https://doi.org/10.1002/aenm.201401142).
- Wu, L.; Buchholz, D.; Bresser, D.; Gomes Chagas, L.; Passerini, S. *J. Power Sources* **2014**, *251*, 379.
- Wu, L.; Moretti, A.; Buchholz, D.; Passerini, S.; Bresser, D. *Electrochim. Acta* **2016**, *203*, 109.
- Bella, F.; Muñoz-García, A. B.; Meligrana, G.; Lamberti, A.; Destro, M.; Pavone, M.; Gerbaldi, C. *Nano Res.* **2017**, *10*, 2891.
- Wang, B.; Zhao, F.; Du, G.; Porter, S.; Liu, Y.; Zhang, P.; Cheng, Z.; Liu, H. K.; Huang, Z. *ACS Appl. Mater. Interfaces* **2016**, *8*, 16009.
- Chen, J.; Ding, Z.; Wang, C.; Hou, H.; Zhang, Y.; Wang, C.; Zou, G.; Ji, X. *ACS Appl. Mater. Interfaces* **2016**, *8*, 9142.
- Wu, F.; Luo, R.; Xie, M.; Li, L.; Zhang, X.; Zhao, L.; Zhou, J.; Wang, K.; Chen, R. *J. Power Sources* **2017**, *362*, 283.
- Zhang, H.; Hasa, I.; Passerini, S. *Adv. Energy Mater.* **2018**, *8*, No. 1702582, DOI: [10.1002/aenm.201702582](https://doi.org/10.1002/aenm.201702582).
- Hasa, I.; Hassoun, J.; Passerini, S. *Nano Res.* **2017**, *10*, 3942.
- Li, J.; Wang, Z.; Zhao, A.; Wang, J.; Song, Y.; Sham, T.-K. *J. Phys. Chem. C* **2015**, *119*, 17848.
- Oh, S.-M.; Hwang, J.-Y.; Yoon, C. S.; Lu, J.; Amine, K.; Belharouak, I.; Sun, Y.-K. *ACS Appl. Mater. Interfaces* **2014**, *6*, 11295.
- Kim, K.-T.; Ali, G.; Chung, K. Y.; Yoon, C. S.; Yashiro, H.; Sun, Y.-K.; Lu, J.; Amine, K.; Myung, S.-T. *Nano Lett.* **2014**, *14*, 416.

- (19) Li, J.; Liu, J.; Sun, Q.; Banis, M. N.; Sun, X.; Sham, T.-K. *J. Phys. Chem. C* **2017**, *121*, 11773.
- (20) Peled, E. *J. Electrochem. Soc.* **1979**, *126*, 2047.
- (21) Eshetu, G. G.; Diemant, T.; Hekmatfar, M.; Grugeon, S.; Behm, R. J.; Laruelle, S.; Armand, M.; Passerini, S. *Nano Energy* **2019**, *55*, 327.
- (22) Xu, Z.-L.; Lim, K.; Park, K.-Y.; Yoon, G.; Seong, W. M.; Kang, K. *Adv. Funct. Mater.* **2018**, *28*, No. 1802099, DOI: [10.1002/adfm.201802099](https://doi.org/10.1002/adfm.201802099).
- (23) Vázquez-Santos, M. B.; Morales, E.; Tartaj, P.; Amarilla, J. M. *ACS Omega* **2017**, *2*, 3647.
- (24) Siebert, A.; Dou, X.; Garcia-Diez, R.; Buchholz, D.; Félix, R.; Handick, E.; Greco, G.; Hasa, I.; Wilks, R. G.; Passerini, S.; Bär, M. *ACS Appl. Energy Mater.* **2021**, *4*, 164.
- (25) Verma, P.; Maire, P.; Novák, P. *Electrochim. Acta* **2010**, *55*, 6332.
- (26) Peled, E.; Menkin, S. *J. Electrochem. Soc.* **2017**, *164*, A1703.
- (27) Dedryvère, R.; Laruelle, S.; Grugeon, S.; Gireaud, L.; Tarascon, J.-M.; Gonbeau, D. *J. Electrochem. Soc.* **2005**, *152*, A689.
- (28) Dedryvère, R.; Gireaud, L.; Grugeon, S.; Laruelle, S.; Tarascon, J.-M.; Gonbeau, D. *J. Phys. Chem. B* **2005**, *109*, 15868.
- (29) Ventosa, E.; Madej, E.; Zampardi, G.; Mei, B.; Weide, P.; Antoni, H.; La Mantia, F.; Muhler, M.; Schuhmann, W. *ACS Appl. Mater. Interfaces* **2017**, *9*, 3123.
- (30) Andersson, A. M.; Henningson, A.; Siegbahn, H.; Jansson, U.; Edström, K. *J. Power Sources* **2003**, *119–121*, S22.
- (31) Späth, T.; Becker, D.; Schulz, N.; Hausbrand, R.; Jaegermann, W. *Adv. Mater. Interfaces* **2017**, *4*, No. 1700567, DOI: [10.1002/admi.201700567](https://doi.org/10.1002/admi.201700567).
- (32) Muñoz-Márquez, M. A.; Zarrabeitia, M.; Castillo-Martínez, E.; Eguía-Barrio, A.; Rojo, T.; Casas-Cabanas, M. *ACS Appl. Mater. Interfaces* **2015**, *7*, 7801.
- (33) Greco, G.; Mazzio, K. A.; Dou, X.; Gericke, E.; Wendt, R.; Krumrey, M.; Passerini, S. *ACS Appl. Energy Mater.* **2019**, *2*, 7142–7151, DOI: [10.1021/acsaem.9b01101](https://doi.org/10.1021/acsaem.9b01101).
- (34) *Handbook of X-ray Photoelectron Spectroscopy: A Reference Book of Standard Spectra for Identification and Interpretation of XPS Data*; Moulder, J. F.; Chastain, J., Eds.; Perkin-Elmer Corporation: Eden Prairie, MN, 1992.
- (35) Yao, K.; Zheng, J. P.; Liang, R. *J. Power Sources* **2018**, *381*, 164.
- (36) Peled, E.; et al. *J. Electrochem. Soc.* **1998**, *145*, 3482 DOI: [10.1149/1.1838831](https://doi.org/10.1149/1.1838831).
- (37) Peled, E.; Bar Tow, D.; Merson, A.; Gladkich, A.; Burstein, L.; Golodnitsky, D. *J. Power Sources* **2001**, *97–98*, S2.
- (38) Balbuena, P. B.; Wang, Y. *Lithium-Ion Batteries: Solid-Electrolyte Interphase*; World Scientific: Singapore, 2004.
- (39) Ponrouch, A.; Dedryvère, R.; Monti, D.; Demet, A. E.; Ateba Mba, J. M.; Croguennec, L.; Masquelier, C.; Johansson, P.; Palacín, M. R. *Energy Environ. Sci.* **2013**, *6*, 2361.
- (40) Vogdanis, L.; Martens, B.; Uchtmann, H.; Hemel, F.; Heitz, W. *Makromol. Chem.* **1990**, *191*, 465 DOI: [10.1002/macp.1990.021910301](https://doi.org/10.1002/macp.1990.021910301).
- (41) Kanamura, K.; Tamura, H.; Takehara, Z. *J. Electroanal. Chem.* **1992**, *333*, 127.
- (42) Dahbi, M.; Nakano, T.; Yabuuchi, N.; Ishikawa, T.; Kubota, K.; Fukunishi, M.; Shibahara, S.; Son, J.-Y.; Cui, Y.-T.; Oji, H.; Komaba, S. *Electrochem. Commun.* **2014**, *44*, 66.
- (43) Kubota, K.; Komaba, S. *J. Electrochem. Soc.* **2015**, *162*, A2538.
- (44) Crowe, R.; Badyal, J. P. S. *J. Chem. Soc., Chem. Commun.* **1991**, *2*, 958 DOI: [10.1039/C39910000958](https://doi.org/10.1039/C39910000958).
- (45) Copperthwaite, R. G.; Lloyd, J. *J. Chem. Soc., Dalton Trans.* **1977**, 1117.
- (46) Rabuni, M. F.; Nik Sulaiman, N. M.; Aroua, M. K.; Hashim, N. *Ind. Eng. Chem. Res.* **2013**, *52*, 15874.
- (47) Krause, M. O.; Oliver, J. H. *J. Phys. Chem. Ref. Data* **1979**, *8*, 329.
- (48) Södergren, S.; Siegbahn, H.; Rensmo, H.; Lindström, H.; Hagfeldt, A.; Lindquist, S.-E. *J. Phys. Chem. B* **1997**, *101*, 3087.
- (49) Saltas, V.; Tonti, D.; Pettenkofer, C.; Jaegermann, W.; et al. *Surf. Rev. Lett.* **2000**, *7*, 235 DOI: [10.1142/S0218625X00000270](https://doi.org/10.1142/S0218625X00000270).
- (50) González, J. R.; Zhecheva, E.; Stoyanova, R.; Nihtianova, D.; Markov, P.; Chapuis, R. R.; Alcántara, R.; Nacimiento, F.; Tirado, J. L.; Ortiz, G. F. *Phys. Chem. Chem. Phys.* **2015**, *17*, 4687.
- (51) Xu, Y.; Lotfabad, E. M.; Wang, H.; Farbod, B.; Xu, Z.; Kohandehghan, A.; Mitlin, D. *Chem. Commun.* **2013**, *49*, 8973.
- (52) Gorgoi, M.; Svensson, S.; Schäfers, F.; Öhrwall, G.; Mertin, M.; Bressler, P.; Karis, O.; Siegbahn, H.; Sandell, A.; Rensmo, H.; Doherty, W.; Jung, C.; Braun, W.; Eberhardt, W. *Nucl. Instrum. Methods Phys. Res., Sect. A* **2009**, *601*, 48.
- (53) Schäfers, F.; Mertin, M.; Gorgoi, M. *Rev. Sci. Instrum.* **2007**, *78*, No. 123102, DOI: [10.1063/1.2808334](https://doi.org/10.1063/1.2808334).
- (54) Gorgoi, M.; Schäfers, F.; Svensson, S.; Mårtensson, N. *J. Electron Spectrosc. Relat. Phenom.* **2013**, *190*, 153.
- (55) Schäfers, F. *J. Large-Scale Res. Facil.* **2016**, *2*, No. 92, DOI: [10.17815/jlsrf-2-92](https://doi.org/10.17815/jlsrf-2-92).
- (56) Keski-Rahkonen, O.; Krause, M. O. *At. Data Nucl. Data Tables* **1974**, *14*, 139.
- (57) Tanuma, S.; Powell, C. J.; Penn, D. R. *Surf. Interface Anal.* **1994**, *21*, 165.
- (58) Shinotsuka, H.; Tanuma, S.; Powell, C. J.; Penn, D. R. *Surf. Interface Anal.* **2015**, *47*, 871.
- (59) Trzhaskovskaya, M. B.; Nefedov, V. I.; Yarzhemsky, V. G. *At. Data Nucl. Data Tables* **2001**, *77*, 97.
- (60) Trzhaskovskaya, M. B.; Nefedov, V. I.; Yarzhemsky, V. G. *At. Data Nucl. Data Tables* **2002**, *82*, 257.
- (61) Trzhaskovskaya, M. B.; Nikulin, V. K.; Nefedov, V. I.; Yarzhemsky, V. G. *At. Data Nucl. Data Tables* **2006**, *92*, 245.
- (62) Streubel, P.; Hesse, R.; Makhova, L.; Schindelka, J.; Denecke, R. *A Practical Method for Thickness Estimation of Ultrathin Layers from XPS Data with UNIFIT* Universität Leipzig: Germany.
- (63) Painter, L. R.; Arakawa, E. T.; Williams, M. W.; Ashley, J. C. *Radiat. Res.* **1980**, *83*, 1.